Acta Cryst. (1999). A**55**, 423–432

X-ray diffraction moiré topography as a means to reconstruct relative displacement fields in weakly deformed bicrystals

M. Ohler,[a,b] S. Köhler[a,c] and J. Härtwig[a]*

[a]*European Synchrotron Radiation Facility, BP 220, F-38043 Grenoble, France,* [b]*Arbeitsgruppe Röntgenbeugung, Institut für Physik, Humboldt-Universität Berlin, Hausvogteiplatz 5-7, D-10117 Berlin, Germany, and* [c]*Mineralogisches Institut der Universität Würzburg, Am Hubland, D-97074 Würzburg, Germany. E-mail: haertwig@esrf.fr*

(*Received 1 April 1998; accepted 13 August 1998*)

Abstract

X-ray diffraction topographs of wafers produced by separation by implanted oxygen (SIMOX) show moiré fringes in both reflection and transmission geometry. These fringes reveal deformations of the order of 10^{-6} to 10^{-8} between the layer and the substrate of the SIMOX material. A new method for a quantitative analysis of moiré fringes is developed and allows reconstruction with a high sensitivity of the three components of the relative displacement field between layer and substrate directly from a set of topographs. This method is used for the interpretation of moiré topographs of entire 4 in SIMOX wafers and of regions around crystal defects. Finally, the capabilities of an analysis of moiré fringes are compared with those of the usual diffraction topography.

1. Introduction

X-ray diffraction moiré fringes have been observed on topographs of *LLL* interferometers (Bonse & Hart, 1965) and of bicrystals (Chikawa, 1965; Lang, 1968). On topographs of wafers produced by the method of separation by implanted oxygen (SIMOX), such fringes were first reported by Jiang *et al.* (1990). The analysis of moiré fringes on X-ray topographs is used for many applications (for a review, see Hart, 1975) and its foundations have recently attracted growing interest (Yoshimura, 1996*a*; Haroutyunyan & Sedrakyan, 1997). In spite of the large number of publications on this subject, almost exclusively the symmetrical transmission (Laue) geometry has been investigated. Little effort has been spent on analysing topographs recorded in an asymmetrical transmission or in a reflection (Bragg) geometry. Recently, Ohler *et al.* (1996) used a series of topographs recorded with symmetrical and asymmetrical transmission reflections to determine six of the nine components of the 'relative strain tensor' between the two parts of a bicrystal. Both crystal parts were supposed to be perfect in this analysis. The aim of the present work is to go one step further and to use the spatial information of the topographs to determine also the spatial variations of the relative strain tensor and the nonlinearities of the relative displacement field between the two parts of the bicrystal. Among other factors, the observation of previously unexplained bent moiré fringes on topographs of SIMOX wafers motivated this work. The theoretical basis for such an analysis was given by Ohler & Härtwig (1999). We would also like to point out that, to the best of our knowledge, for the first time the reflection geometry is extensively employed here to record diffraction moiré patterns and that sets of moiré patterns are used to reconstruct the relative displacement field between the two parts of a bicrystal. This is a special example for the solution of an inverse problem, that is for the calculation of a lattice deformation directly from contrast distributions in a set of X-ray topographs.

2. Samples and experimental methods

In the experiments of the present study, bicrystals produced with the SIMOX method were used. For this method, commonly and also for the samples investigated here, 550 μm thick Czochralski-grown silicon wafers, each with a [001] surface normal, are used. The SIMOX process (Badaw & Anand, 1977) consists of an oxygen-ion implantation into silicon and a subsequent heat treatment. It leads to the formation of a monocrystalline silicon layer on top of an amorphous SiO_x layer ($x \simeq 2$) on top of a silicon substrate. The defect structure of such 'standard' samples has been investigated by Prieur, Guilhalmenc *et al.* (1996), among others. Other samples were obtained from the same initial silicon material but with a multiple oxygen implantation ('multi-implantation') process (*e.g.* Veneables *et al.*, 1992). For both the standard and the multi-implantation material studied here, the SiO_x layer is 0.4 μm thick, whereas the thickness of the silicon layer originally is 0.2 μm. On many samples, this thickness was increased by chemical vapour deposition to thicknesses from 1 μm up to 15 μm. A sketch of the SIMOX structure is given in Fig. 1. Most of the studied samples were quarter cuts from 4 in SIMOX wafers but also entire 4 in wafers were analysed. Like most heterostuctures, SIMOX wafers are

bent; typical bending radii ranged between 50 and 100 m.

X-ray diffraction topography is a well established method to image defects in crystalline materials (Bowen & Tanner, 1998). For the present work, topographs have been recorded in both transmission and reflection geometries.

The transmission topographs were taken at the ID19 topography beamline, a wiggler beamline of the ESRF that provides X-ray energies between about 8 and 140 keV. The source size is about 130 × 50 μm horizontal × vertical. The experimental station is 145 m downstream from the source and a beam size up to 45 × 15 mm horizontal × vertical can be used. The small source size and the large distance between the source and the sample lead to a high spatial resolution of the topographs recorded at this beamline, even for large sample-to-film distances. For example, for our white-beam experiments (see Fig. 2*a*), typical sample-to-film distances were 17–20 cm (but could also be much larger). This was necessary to separate the diffracted beams. For such a set-up, the geometrical resolution of the measurement is much better than 1 μm. All transmission topographs shown in this work were recorded with white synchrotron radiation. However, to check the nature of the observed fringes, other topographs, not presented here, were also recorded with double-crystal set-ups. Therefore, mostly a symmetrical 111 transmission monochromator was used. The topographs were then taken with 220 or 111 reflections in symmetrical or asymmetrical transmission geometry, respectively. Two kinds of films were used as detectors. The faster Kodak INDUSTREX SR, and the slower but high-resolution Kodak SO-343 with a developed unexposed grain size of about 40 nm (Prieur & Cloetens, 1996). After exposure and development, the resolution of the first film was a few micrometres, and that of the second film was not much better than 1 μm. The exposure times were of the order of sub-seconds or seconds for the SR film, and a minute or several minutes for the SO-343.

In the reflection geometry, the topographs were recorded with the Cu $K\alpha_1$ radiation from an X-ray tube using a curvable 224 monochromator/collimator crystal to adapt to the sample bending (Jenichen *et al.*, 1985, 1988). Fig. 2(*b*) shows this set-up. Such a topography camera is particularly suited to the study of semiconductor heterostructures. It is also constructed so that the X-ray source can be rotated in a way that the sample is held horizontally and in this way the mounting does not introduce additional stress. Thanks to an asymmetric cut of the monochromator/collimator crystal, samples with a diameter of up to 10 cm can be entirely imaged with this camera. Both ORWO TF 10 films, with resolutions of 10–20 μm, and Ilford L4 nuclear plates, with a typical resolution of 1 μm, have been used to record the images. The film material was always mounted parallel to the crystal surface. The topographs of the 4 in wafers were recorded with the ORWO TF 10 films within an exposure time of 5 to 10 min. The exposure time of the nuclear plates ranged between 3 and 6 h. Depending on the reflection used and the beam size needed to illuminate the sample, the sample-to-film distances ranged between 1 and 2.5 cm. For the smaller distances, a geometrical resolution of 1 μm can be achieved.

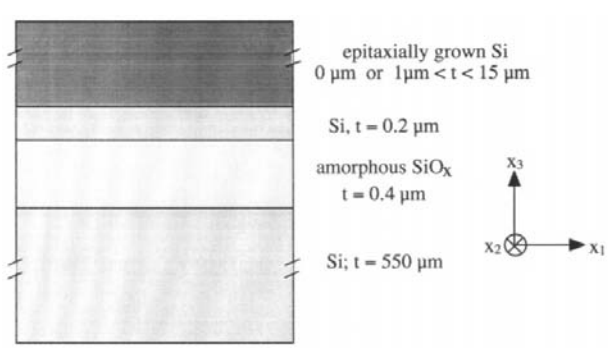

Fig. 1. A vertical cut through the SIMOX structure of the studied samples, with thicknesses t of the individual layers, and the coordinate system used.

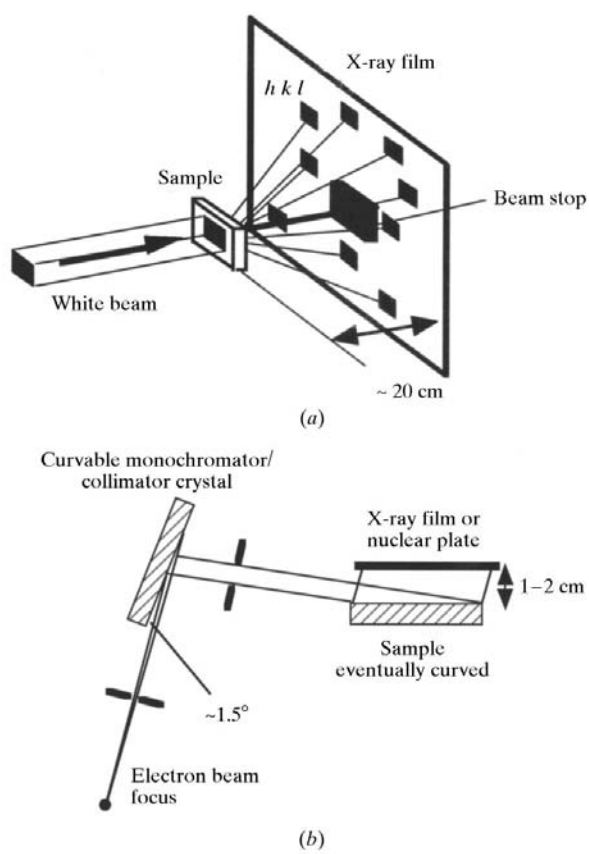

Fig. 2. The experimental techniques used in the present study: (*a*) white-beam topography using synchrotron radiation and (*b*) curvable monochromator topography at a laboratory source.

3. Experimental results

On most of the topographs, recorded with white or monochromatic radiation, in transmission or reflection geometry, pronounced interference fringes could be seen. The nature of these fringes was first checked by etching away part of the layer on some samples. These regions did not give rise to fringes on the topographs. This can, for example, be seen on the topograph of Fig. 3. It is also a typical example of the moiré fringes recorded in reflection geometry. Moreover, in none of our experiments could fringes be observed on samples with a 0.2 μm thick layer, but they were clearly detected on transmission and reflection topographs of samples with a layer thickness of 1 μm or more. This means that at least a layer thickness between 0.2 and 1 μm is needed to observe fringes on X-ray topographs recorded with our experimental methods. The interfringe distance ranged between several hundreds of micrometres and several millimetres, but for a given sample the fringe spacing was significantly smaller on 224 and 004 reflections than on 220 or 004 transmission topographs. The fringes were also independent of the selected wavelength. For the double-crystal topographs, in both reflection and transmission geometries, the fringe pattern did not depend on the angular deviation from the maximum reflectivity position. Moreover, the distance between the fringes shrank to $1/n$th of the initial value when the nth harmonic was used to record the topograph. The fringe contrast was strongest for layer thicknesses between 1 and 5 μm in the reflection geometry (using the Cu $K\alpha_1$ radiation) and for layer thicknesses of about 10 μm or more in the transmission geometry (selecting wavelengths of typically 0.3 Å). The fringes were straight and had an almost constant spacing between them on almost all topographs recorded in the symmetrical transmission geometry. For an asymmetrical transmission geometry, the fringes were often bent. On topographs in reflection geometry, they showed a complex pattern but the topographs of entire SIMOX wafers displayed a remarkable symmetry. This is seen on the topographs of Figs. 4(*a*)–4(*d*), where the contrast recorded on the TF10 films was reduced to a pure black-and-white contrast. For example, a topograph recorded with the $2\bar{2}4$ reflection is very similar to the one recorded with the 224 reflection when it is rotated by 90°, the one obtained with the $\bar{2}\bar{2}4$ reflection must be rotated by 180° and the one of the $\bar{2}24$ reflection by −90° to obtain comparable similarities. These symmetries reflect a fourfold symmetry of the sample around the [001] surface normal. For geometrical reasons, the 4 in wafers could not be imaged on a single topograph recorded in the symmetrical reflection geometry. However, such topographs of the quarter pieces of 4 in wafers indicate a similar circular symmetry around the centre of the wafer.

In some regions of the samples, defects were present. The influence on the fringe pattern of threading dislocation pairs, typical for SIMOX, or of single dislocations has been discussed in detail by Prieur, Guilhalmenc *et al.* (1996) and Prieur, Ohler & Härtwig (1996). Moreover, the topograph presented in Fig. 3 also shows a remarkable discontinuity, a step in the moiré pattern. Such steps could also be observed on topographs of several other samples but they were not related to the inhomogeneities in the samples revealed by chemical etching experiments. Other defects in the SIMOX material with an epitaxic silicon layer were related to agglomerations of stacking faults, decorated with pairs of threading dislocations. Such defects give rise to dipole-like additional interference fringes (see Fig. 5) on all topographs except those recorded in the symmetrical reflection geometry.

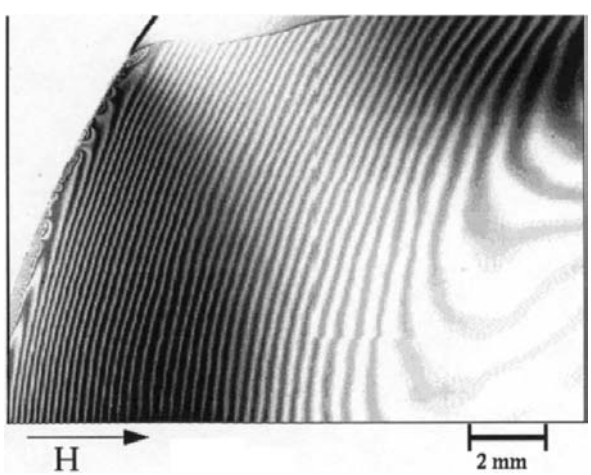

Fig. 3. Moiré pattern on a 422 topograph of a multi-implantation SIMOX wafer recorded in reflection geometry. Layer thickness 5 μm, $\lambda = 1.5$ Å.

4. Interpretation of the topographs

The experimental findings clearly show that the observed interference fringes are moiré fringes. This has also been demonstrated in an earlier work (Ohler *et al.*, 1996) with additional experiments. In particular, for the samples studied here, variations of the Si and the SiO_x layer and the Si substrate thicknesses cannot influence the fringe pattern. Such an influence could be due to the *Pendellösung* effect. For the transmission experiments, the *Pendellösung* length was typically about 60 μm. This is much more than the variations of any of the thicknesses. In the reflection geometry, the *Pendellösung* length was about 10 μm for the 422 reflection. It is much larger than the Si and the SiO_2 layer thickness. Thus, the thickness variations do not reach the scale of the *Pendellösung* length and, together with the other findings, the fringe patterns can be attributed to the moiré effect. Detailed analyses of situations in which the gap

and the layer thicknesses can influence the fringe pattern are given by Yoshimura (1991) and Haroutyunyan (1996), respectively.

In most of the published work on the diffraction moiré effect, the analysis of the fringes is performed with analogy to the superposition of optical gratings. This is obviously correct for topographs of perfect bicrystals recorded in symmetrical transmission geometry. It can then be shown that for an identical reflecting lattice plane spacing d in both parts of the bicrystal and a rotation with an angle α between them, the moiré fringes are *perpendicular* to the reflecting lattice planes and have an interfringe spacing of $D = d/\alpha$. When the spacings of the reflecting lattice planes differ by Δd, and in the absence of a rotation, the moiré fringes are *parallel* to the reflecting lattice planes and have a spacing of $D = d^2/\Delta d$. By measurement of the moiré fringe spacing perpendicular and parallel to the lattice planes on an X-ray topograph, both these contributions can be evaluated.

This description is only valid when the topograph of a perfect bicrystal is recorded in symmetrical transmission geometry (symmetrical Laue case). For an asymmetrical transmission geometry, Ohler *et al.* (1996) have shown that a new moiré fringe arises whenever $\Delta\mathbf{H} \cdot (\mathbf{r} - \mathbf{r}_0)$ equals an integer. In this expression, $\mathbf{r}$ is an observation point and $\mathbf{r}_0$ a reference point, both in the crystal surface, and $\Delta\mathbf{H} = -\text{grad}[\mathbf{H} \cdot \mathbf{u}(\mathbf{r})]$ is the difference between the reciprocal-lattice vectors of the two parts of the bicrystal. Here, $\mathbf{u}(\mathbf{r})$ is the displacement field of the atoms in one part of the bicrystal referred to the positions of the atoms in the other part, the relative displacement field. Note that $\mathbf{u}(\mathbf{r})$ is a linear function in $\mathbf{r}$ for a perfect bicrystal. This description of the moiré fringes implies that the component of $\Delta\mathbf{H}$ perpendicular to the sample surface cannot be determined from the moiré pattern, which also follows from symmetry considerations (Ohler *et al.*, 1996). Moreover, only the length and the direction but not the sign of the component of $\Delta\mathbf{H}$ parallel to the sample surface, called $\Delta\mathbf{H}_{\|}$ from now on, can be determined from the moiré fringes.

In addition, Ohler & Härtwig (1999) showed that moiré fringes on X-ray topographs of perfect bicrystals

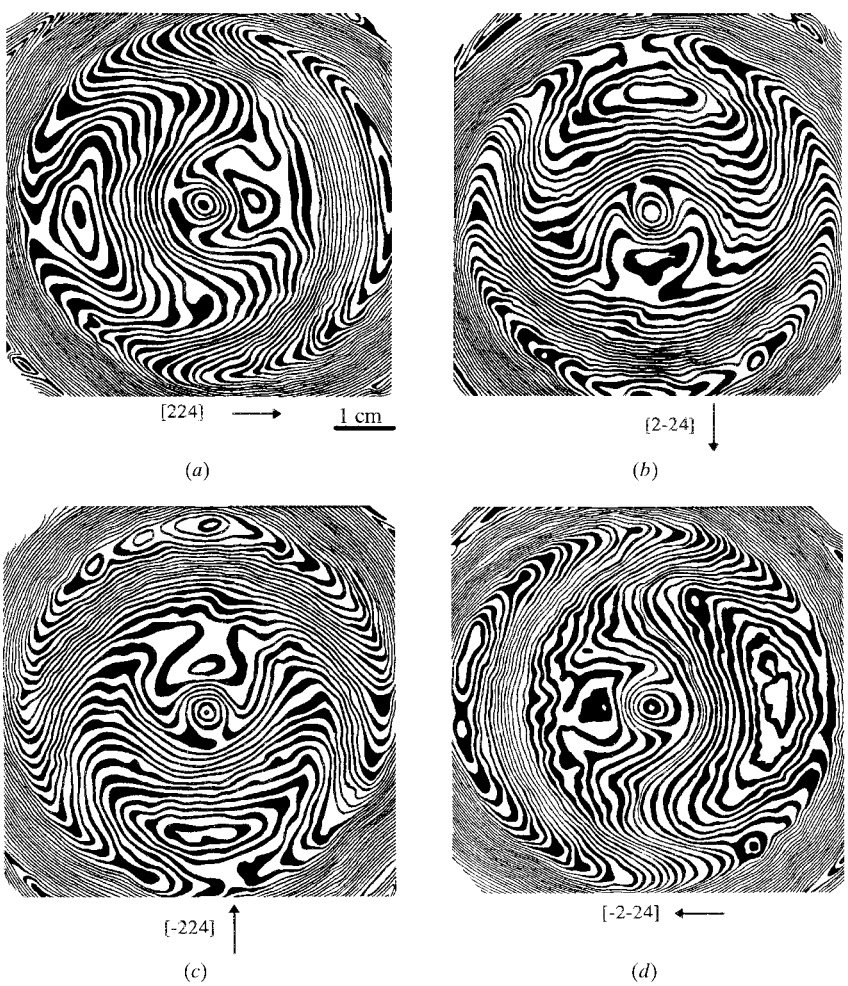

Fig. 4. Moiré patterns on four 422 topographs of a 4 in standard SIMOX wafer recorded in reflection geometry. The original grey levels on the topographs have been reduced to a pure black-and-white contrast for further analysis. Layer thickness 5 μm, $\lambda = 1.5$ Å.

recorded in the reflection geometry can be analysed in the same way as those recorded in the transmission geometry. This means that the moiré fringes on an X-ray topograph of a perfect bicrystal, recorded in any geometry, are perpendicular to $\Delta\mathbf{H}_{\|}$ and have a spacing of $D = |\Delta\mathbf{H}_{\|}|^{-1}$.

When analysing at least three different moiré topographs, one can determine those six of the nine components of the relative deformation tensor $\varepsilon_{ij}(\mathbf{r}) = \partial u_j(\mathbf{r})/\partial x_i \;\; (i, j = 1, 2, 3)$ that are due to the derivations of $u_j(\mathbf{r})$ with respect to the directions parallel to the sample surface, x_1 and x_2. For the coordinate system used, see Fig. 1. Like the component ΔH_3, the component of $\Delta\mathbf{H}$ that is perpendicular to the sample surface, the three components ε_{31}, ε_{32} and ε_{33} cannot be determined from the moiré fringes. In addition, as the sign of $\Delta\mathbf{H}_{\|}$ cannot be found, the global sign of ε_{ij} cannot be determined either. Now, for example for cubic crystals, the reciprocal-lattice-vector difference is related to the relative deformation tensor by $\Delta H_i = -\sum \varepsilon_{ij} h_j / a_0$, where the h_i are the Miller indices of the reflection, a_0 is the lattice parameter and the $u_i(\mathbf{r})$ and ΔH_i are the components in the x_i direction of $\mathbf{u}(\mathbf{r})$ and $\Delta\mathbf{H}$, respectively. With an integration over a direction of observation parallel to the sample surface, $\mathbf{r}_{\|} = (x_1, x_2, 0)$, one can find the function $\mathbf{u}(\mathbf{r}_{\|})$. The dependence of $\mathbf{u}(\mathbf{r})$ on the direction perpendicular to the sample surface and also the sign of $\mathbf{u}(\mathbf{r}_{\|})$ cannot be determined from the moiré fringes.

This previous description has further been generalized by Ohler & Härtwig (1999) for the case of a bicrystal composed of one perfect and another weakly deformed and locally perfect part. For such a 'locally perfect bicrystal', the deformed crystal part is thin and the deformation only gives rise to a shift of the Bragg angle, which is much smaller than the width of the reflection curve. Moreover, $\mathbf{u}(\mathbf{r})$ is a slowly varying function in $\mathbf{r}$ and consequently $\Delta\mathbf{H}$ is not constant. This means that the previously used expression $\Delta\mathbf{H} \cdot (\mathbf{r} - \mathbf{r}_0)$ must be replaced by $\int \Delta\mathbf{H}(\mathbf{r}_{\|}) \cdot \mathrm{d}\mathbf{r}_{\|}$, which results in the 'moiré phase' $\Phi_M(\mathbf{r}_{\|}) = -\mathbf{H} \cdot \mathbf{u}(\mathbf{r}_{\|})$ plus a constant phase Φ_0. Here, $\mathbf{u}(\mathbf{r}_{\|})$ can be an arbitrary slowly varying function. Also for a weakly deformed bicrystal, the sign of $\mathbf{u}(\mathbf{r})$ and its dependence on the direction perpendicular to the sample surface cannot be determined from the moiré fringes. A rigid-body translation $\mathbf{u}_0$ of one crystal lattice with respect to the lattice of the other plate of the bicrystal influences Φ_0, which is constant over the entire sample, does not lead to any contrast on the topograph and cannot be determined from the fringe pattern. Now, a new moiré fringe then arises each time the moiré phase equals an integer. The previous formulation for perfect bicrystals, for which $\Delta\mathbf{H} \cdot (\mathbf{r} - \mathbf{r}_0)$ must be an integer for a new moiré fringe to appear, is a special case of the more general situation of a locally perfect bicrystal for which $-\mathbf{H} \cdot \mathbf{u}(\mathbf{r}_{\|})$ must be an integer at each moiré fringe.

The information about the relative displacement field $\mathbf{u}(\mathbf{r}_{\|})$ is contained in the intensity profile of the moiré fringes. In the transmission geometry, a modulation of the intensity with $\cos[2\pi\Phi_M(\mathbf{r}_{\|})]$ is expected, whereas, in the reflection geometry, the intensity profile of a moiré fringe depends in a complicated way on the experimental conditions (Ohler & Härtwig, 1999). The simplest way to interpret moiré fringes recorded in reflection and transmission geometries is to sample the intensity pattern such that one fringe only consists of two intensities, its maximum and minimum values. This means that the grey levels of the topographs are translated into a pure black-and-white contrast. Then it is also possible to interpret in the same way moiré fringes recorded either in transmission or in reflection geometry. However, now the spatial resolution of the information extracted from the topographs is not better than half the distance of a moiré fringe. To increase the spatial resolution, the method presented in the following

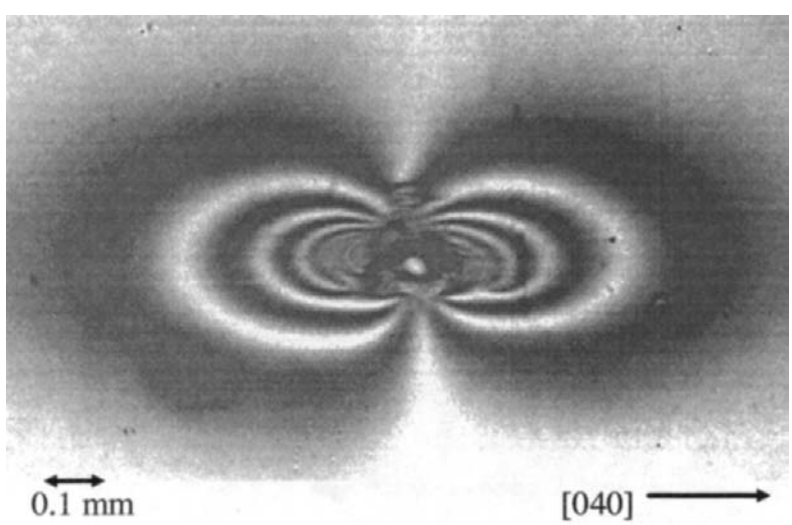

Fig. 5. White-beam transmission topograph of a standard SIMOX wafer, showing dipole-like additional moiré fringes due to agglomerations of stacking faults and of several pairs of dislocations with antiparallel Burgers vectors. 040 reflection. Layer thickness 5 μm, $\lambda = 0.3$ Å.

must be further developed to also take into account the intensity profile of the fringes.

Now, such black-and-white topographs, like those of Fig. 4, consist of lines where the moiré phase is constant, namely the moiré fringes. The levels of the moiré phase $\Phi_M(\mathbf{r}_\parallel)$ differ by $\pm\frac{1}{2}$ from a black to a white and from a white to a black moiré fringe. This provides, in principle, the possibility to reconstruct the $\mathbf{u}(\mathbf{r}_\parallel)$ from the $\Phi_M(\mathbf{r}_\parallel)$. Therefore, one can look upon the moiré fringes as the contour lines of a '$\Phi_M(\mathbf{r}_\parallel)$ map'. This is comparable to a topographic map with the contour lines of a mountain for example. The aim of the analysis of moiré fringes then is to find the 'height' of each contour line, *i.e.* of each moiré fringe. This procedure provides the moiré phase $\Phi_M(\mathbf{r}_\parallel)$ from the moiré fringes. On each topograph, the moiré phase $\Phi_M(\mathbf{r}_\parallel) = -\mathbf{H}\cdot\mathbf{u}(\mathbf{r}_\parallel)$ is a projection of $\mathbf{u}(\mathbf{r}_\parallel)$ on the diffraction vector $\mathbf{H}$. To determine the three components of $\mathbf{u}(\mathbf{r}_\parallel)$, one needs at least three such projections. When the $\Phi_M(\mathbf{r}_\parallel)$ on more than three individual topographs have been determined from the moiré fringes, they can also be checked for consistency: the components of $\mathbf{u}(\mathbf{r}_\parallel)$ calculated from the $\Phi_M(\mathbf{r}_\parallel)$ in different ways must agree among themselves.

Unfortunately, such a reconstruction of $\mathbf{u}(\mathbf{r}_\parallel)$ from moiré topographs is not straightforward because moiré fringes, like any contour lines, have several ambiguities. Firstly, on a given topograph, 'ridges' of the moiré phase $\Phi_M(\mathbf{r}_\parallel)$ cannot be distinguished from 'valleys'. This is schematically demonstrated in Fig. 6. The possibilities for the function $\mathbf{H}\cdot\mathbf{u}(\mathbf{r}_\parallel)$ shown there are only two out of many others to produce the same moiré pattern. However, comparison of topographs recorded with different reflections shows that such ambiguities can, in principle, be overcome. On the other hand, $\Phi_M(\mathbf{r}_\parallel)$ and $-\Phi_M(\mathbf{r}_\parallel)$ as well as $\Phi_M(\mathbf{r}_\parallel)$ and $\Phi_M(\mathbf{r}_\parallel)+\Phi_0$ lead to the same moiré pattern – and these ambiguities cannot be overcome. This means, as already stated, that a rigid-body translation $\mathbf{u}_0$ and also the sign of $\mathbf{u}(\mathbf{r}_\parallel)$ cannot be found from the moiré fringes.

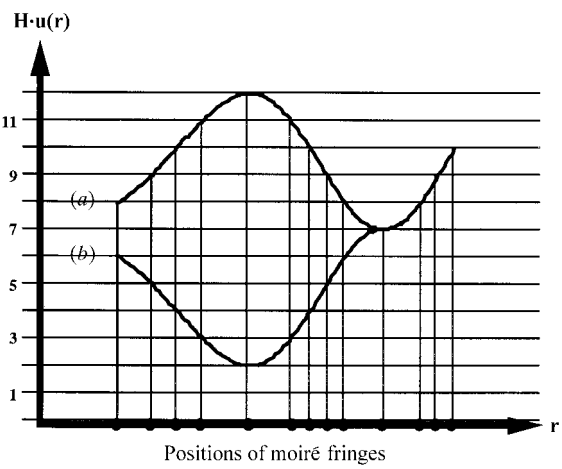

Fig. 6. Relation between the function $\mathbf{H}\cdot\mathbf{u}(\mathbf{r})$ along a given direction in a moiré pattern and the location of the fringes: each time $\mathbf{H}\cdot\mathbf{u}(\mathbf{r})$ equals an integer, a new moiré fringe is introduced in the pattern. The two possibilities (*a*) and (*b*), out of many others that produce the same moiré pattern, can only be distinguished when several topographs with different diffraction vectors $\mathbf{H}$ are analysed.

The moiré phases on the different topographs can be written as $\Phi_{M,i}(\mathbf{r}_\parallel) = -\sum h_{ij}u_j(\mathbf{r}_\parallel)$ with $\mathbf{H}_i = (h_{i1}, h_{i2}, h_{i3})$ for the diffraction vector of the ith topograph. If the moiré phases $\Phi_{M,i}(\mathbf{r}_\parallel)$ were known and not only the corresponding contour lines, *i.e.* the moiré fringes, then the $u_i(\mathbf{r}_\parallel)$ could be calculated by inverting the matrix h_{ij}:

$$u_i(\mathbf{r}_\parallel) = -\sum h^*_{ij}\Phi_{M,i}(\mathbf{r}_\parallel), \qquad (1)$$

where h^*_{ij} is the inverse of the matrix h_{ij}.

However, to do this, one first needs to attribute a 'height' to all fringes on each moiré pattern; this means that the moiré phase on each topograph has to be determined.

We have developed a procedure to obtain consistent moiré phases $\Phi_M(\mathbf{r}_\parallel)$ from a set of topographs recorded on different reflections. This procedure is based on a trial-and-error method and starts with the physically simplest guess on the moiré phases. Its different steps can be summarized as follows:

(i) Separate the contrast variations due to the moiré fringes from other contrast variations like inhomogeneous illumination of the topograph. This can, for example, be achieved by a filtering of the spatial frequencies that constitute the images.

(ii) 'Digitalize' the intensity of the moiré fringes such that only two intensities, 'black' and 'white', appear on the topographs. Figs. 4(*a*)–4(*d*) show fringe patterns obtained in this way. Sometimes, especially for small fringe spacings, our computer program did not recognize some parts of a fringe and connected, for example, the neighbouring black fringes across the white fringe between them. These errors have to be corrected very carefully, otherwise a meaningful 'height profile' cannot be attributed to the fringes.

(iii) As a rigid-body translation cannot be determined, one can choose an arbitrary point on the sample for the 'height' $\Phi_M(\mathbf{r}_\parallel) = 0$. It may be convenient to choose a point where the fringe spacing on all topographs is large, as for example in the centre of the topographs in Fig. 4.

(iv) From this point, attribute 'height levels' to the moiré fringes in steps of $\frac{1}{2}$ from a black to a white and from a white to a black fringe in such a way that the moiré phases $\Phi_{M,i}(\mathbf{r}_\parallel)$ are as monotonic as possible [*e.g.* possibility (*b*) in Fig. 6]. This corresponds to the physically simplest guess for the $\Phi_{M,i}(\mathbf{r}_\parallel)$.

(v) Use equation (1) to calculate the $u_i(\mathbf{r}_\parallel)$ from the resulting moiré phases $\Phi_{M,i}(\mathbf{r}_\parallel)$. When more than three different topographs are recorded, this may be possible in several ways.

(vi) Compare the different solutions for the $u_i(\mathbf{r}_\parallel)$, for example by displaying them all together on the computer screen. If it improves the agreement between the solutions for $u_i(\mathbf{r}_\parallel)$, invert the sign of the moiré phases on one or more topographs. Isolate in this way the regions where the different solutions for the $u_i(\mathbf{r}_\parallel)$ start to disagree. Up to these regions, the assumption of monotonic moiré phases could explain the fringe patterns. Beyond these regions, this is not possible. If, for example, the moiré phase was increasing until then, let it decrease and *vice versa*. Often it is easy to see on which topographs this should be tried: like the contour levels on a map, most commonly the moiré phase does not vary much close to such local maxima or minima and thus the fringes are more spread out at these places. When this procedure is continued, a solution is found when the agreement between the different solutions for the $u_i(\mathbf{r}_\parallel)$ is better than at least one lattice parameter over the entire sample.

This procedure provides the physically simplest solution that has the least local maxima and/or minima of the moiré phases. Consequently, it also leads to the simplest possible solution for the relative displacement field. However, we have not found a proof that it is also the unique solution. This means that other solutions for the $u_i(\mathbf{r}_\parallel)$, 'going up and down' more often, may be possible. However, one can, at least in principle, test all these possibilities: as the 'height difference' between neighbouring black and white moiré fringes must be $\pm\frac{1}{2}$, there is only a finite number of possibilities to construct the moiré phase from a given moiré pattern. In principle, a moiré fringe pattern could also arise from a moiré phase oscillating between two values when going from one fringe position to the next. This would correspond to the 'most complicated' moiré phase. As long as a proof of the uniqueness of the found solution cannot be given or if it is too time demanding to test all other possibilities, one must ask whether the resulting relative displacement field $\mathbf{u}(\mathbf{r}_\parallel)$ is physically meaningful. Moreover, the result should also be checked with one or more topographs of other reflections that have not been included in the analysis. For example, the 4 in SIMOX wafer has been analysed with the four 224 reflection topographs presented in Fig. 4 and the results have then been checked with two 220 and two 400 transmission topographs of the same sample.

5. Results

5.1. *Reconstruction of the relative displacement field between two crystal plates*

Fig. 4 shows the moiré fringes, reduced to a black-and-white contrast, of the four 224 topographs recorded from a 4 in standard SIMOX wafer. Thus, for the determination of the three components $u_i(\mathbf{r}_\parallel)$ of $\mathbf{u}(\mathbf{r}_\parallel)$, we disposed of one topograph more than absolutely necessary. In general, four different topographs would allow us to calculate the $u_i(\mathbf{r}_\parallel)$ in four ways using equation (1), but owing to the symmetry of the 224 reflections this can only be performed in two ways. Then, the moiré phases $\Phi_{M,hkl}(\mathbf{r}_\parallel)$ were determined with the procedure described before; Fig. 7 shows the moiré phase of the $2\bar{2}4$ topograph of Fig. 4. The moiré phases of the other 224 topographs are very similar to this one when they are rotated by 90, 180 and -90° around the vertical axis. These moiré phases lead to the differences $\delta u_i(\mathbf{r}_\parallel)$ between the two solutions for the $u_i(\mathbf{r}_\parallel)$ that are $\langle\delta u_1(\mathbf{r}_\parallel)\rangle = \langle\delta u_2(\mathbf{r}_\parallel)\rangle = \langle\delta u_3(\mathbf{r}_\parallel)\rangle/2 \simeq 1$ Å. Here, $\langle x(\mathbf{r}_\parallel)\rangle$ means $x(\mathbf{r}_\parallel)$ averaged over the sample. The results obtained for the $u_i(\mathbf{r}_\parallel)$ are displayed in Fig. 8. As seen in this figure, the two in-plane components $u_1(\mathbf{r}_\parallel)$ and $u_2(\mathbf{r}_\parallel)$ are essentially linear functions where $u_1(\mathbf{r}_\parallel)$ varies mainly along the x_1 direction and $u_2(\mathbf{r}_\parallel)$ mainly along the x_2 direction. The component $u_3(\mathbf{r}_\parallel)$, perpendicular to the sample surface, presents a circular symmetry and a dip in the centre of the wafer.

Now six of the nine components of the relative strain tensor $\varepsilon_{ij}(\mathbf{r}_\parallel) = \partial u_j(\mathbf{r}_\parallel)/\partial x_i$ can be calculated from the derivatives of $u_j(\mathbf{r}_\parallel)$ with respect to the two directions of observation, x_1 and x_2. Therefore, the functions $u_j(\mathbf{r}_\parallel)$ are first smoothed over the width of a moiré fringe spacing in order to suppress the steps due to the black-and-white contrast on the topographs. As $u_1(\mathbf{r}_\parallel)$ and $u_2(\mathbf{r}_\parallel)$ are linear functions in $\mathbf{r}_\parallel$, the in-plane dilational components are almost constant over the sample and are found to be $\langle\varepsilon_{11}(\mathbf{r}_\parallel)\rangle = 4.8\ (7) \times 10^{-8}$ and $\langle\varepsilon_{22}(\mathbf{r}_\parallel)\rangle = 4.4\ (9) \times 10^{-8}$, while both the rotation and the shear distortion are much smaller: $\frac{1}{2}\langle\varepsilon_{12}(\mathbf{r}_\parallel) - \varepsilon_{21}(\mathbf{r}_\parallel)\rangle = 0.1\ (8) \times 10^{-8}$ and $\frac{1}{2}\langle\varepsilon_{12}(\mathbf{r}_\parallel) + \varepsilon_{21}(\mathbf{r}_\parallel)\rangle = 0.4\ (7) \times 10^{-8}$. These results are typical for standard SIMOX wafers and correspond well to those obtained from moiré fringes recorded on the two 220 and two 400 transmission topographs of a smaller area of the sample. However, here direct

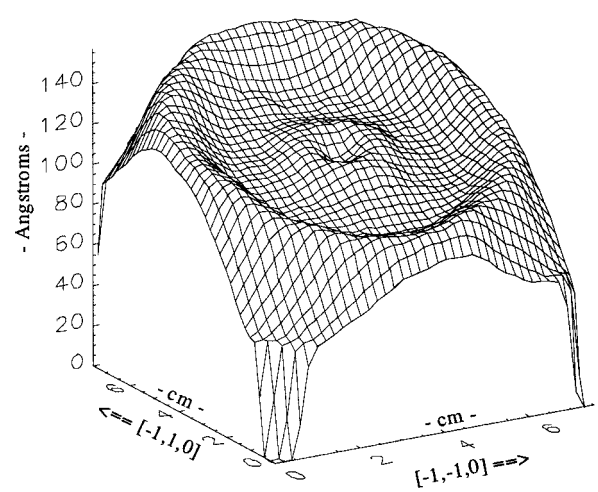

Fig. 7. The moiré phase obtained from the $2\bar{2}4$ topograph of Fig. 4 with the method described in the text.

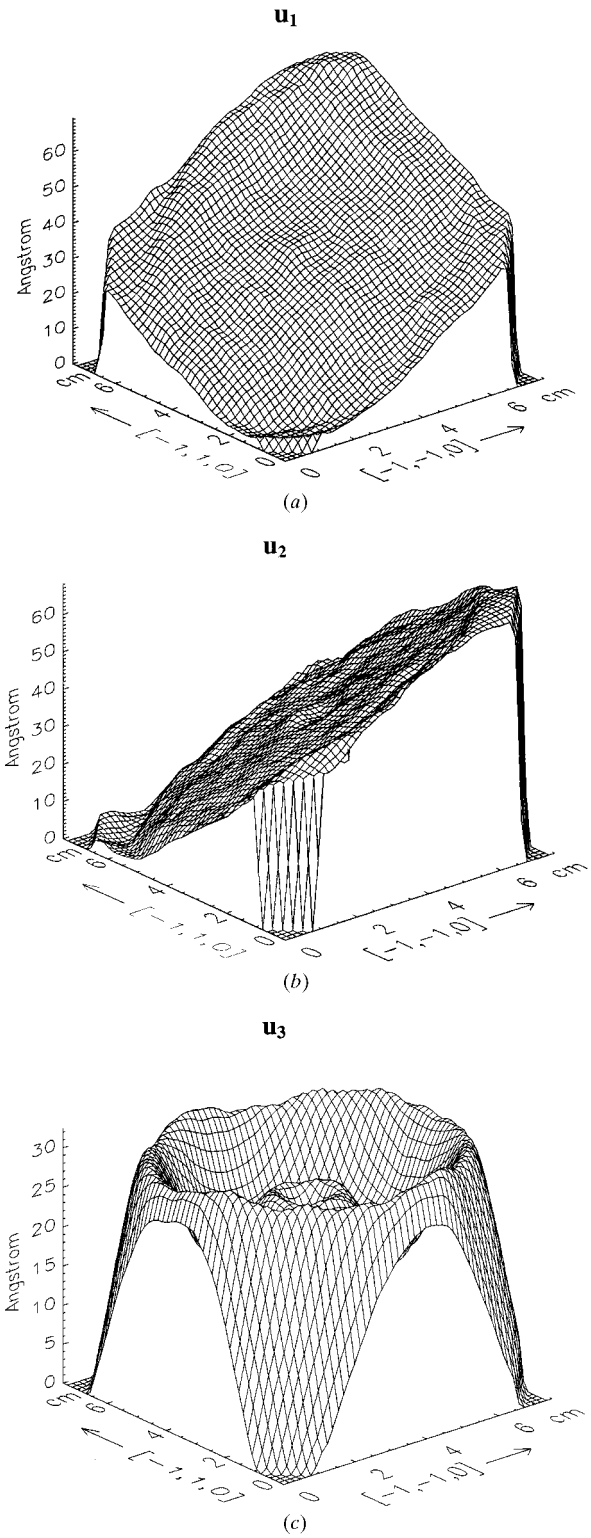

Fig. 8. The components $u_1(\mathbf{r})$, $u_2(\mathbf{r})$ and $u_3(\mathbf{r})$ of the relative displacement field between the layer and the substrate reconstructed from the topographs of Fig. 4.

evidence is found that these components are almost constant over entire 4 in SIMOX wafers, whereas the other components of the relative strain tensor, obtained from the derivatives of the component $u_3(\mathbf{r})$, depend on the location on the sample.

Then, topographs of quarter pieces of standard and multi-implantation SIMOX wafers were recorded in symmetrical and asymmetrical reflection geometries and also in transmission geometry, and were analysed in the same way as described above. All these samples showed the same general features as observed before: the in-plane components of the relative displacement field are linear functions and the out-of-plane component shows a circular symmetry and a dip in the centre of the SIMOX wafer. Moreover, the triple implantation and the standard samples can be distinguished by values of ε_{ii} that are about 2–5 times larger for the multi-implantation material than for the standard SIMOX material.

5.2. *Reconstruction of the relative displacement field around crystal defects*

The method presented before can also be employed to analyse quantitatively the moiré fringes around crystal defects. If the lattice of one part of the bicrystal can be assumed to be perfect, this allows the displacement field around a defect in the other part to be reconstructed without assuming any model. However, this can only be performed with the restrictions of the present method that were discussed above.

For example, the spatial resolution is given by the density of the fringes on the topograph. This has severe implications for the study of dislocations with the method proposed in this article. It is well known that a dislocation with a Burger's vector **b**, situated in one of the parts of a bicrystal, gives rise to $N = \mathbf{H} \cdot \mathbf{b}$ additional fringes on the topograph (Hart, 1972). However, these fringes follow the direction of the surrounding ones and the spatial resolution of the reconstructed relative displacement field around the dislocation is very low. For such cases, the fine details of the contrast on the topograph can be used to extract more information on the relative displacement field. This is not performed by the method proposed here but it has been performed in an analysis by Prieur, Ohler & Härtwig (1996), comparing the observed contrast to the contrast expected for a model deformation field.

On one of our topographs, the $\bar{2}\bar{2}4$ topograph of Fig. 4, we have also observed an unusual dislocation-like discontinuity of the moiré patterns. However, a careful check has shown that this discontinuity did not correspond to any dislocation present in the sample. Such 'pseudo-moiré dislocations' have been observed and studied in detail by Yoshimura (1996*b*), but their origin is still a matter of discussion. We have not investigated in more detail this additional fringe but have suppressed it

for the analysis by setting its moiré phase to that of the surrounding moiré fringe. If this additional fringe really were due to a dislocation, such an omission of an additional fringe would correspond to neglecting a single dislocation in the entire sample. It can thus be assumed that the error made by this simplification is very small for the reconstruction of the relative displacement field.

Except these problems concerning dislocations and 'pseudodislocations', the method presented could successfully be applied to the study of defects. For example, the topograph of Fig. 3 shows a rectangular area where the moiré pattern is dislocated with respect to the surrounding fringes. This 'phase jump' is not constant but equals about $\Delta N \simeq 20\%$ of the moiré fringe spacing. It increases with an increasing component h_3 of the diffraction vector perpendicular to the sample surface and vanishes for $h_3 = 0$ on symmetrical transmission topographs. It can thus be concluded that this phase jump in the moiré pattern is related to a step mainly in the component $u_3(\mathbf{r})$ with a height of only $\Delta u_3 = \Delta N/h_3 \simeq 0.3$ Å. Such steps have been observed on several SIMOX samples; they tend to align along $\langle 011 \rangle$ directions and are well defined over distances up to about 1 cm. However, the origin of such defects is not clear and most probably they can only be observed with methods that are as sensitive to a relative displacement of the crystal lattice as the moiré effect.

Another typical defect image on moiré topographs of SIMOX samples is shown in Fig. 5. Chemical etching and scanning tunnelling microscopy have shown that such defects are related to the epitaxic growth of silicon and not to the SIMOX process itself. These defects consist of agglomerations of stacking faults and of several pairs of dislocations with antiparallel Burgers vectors. They are hardly visible on symmetrical reflection topographs and one can thus conclude that $u_3(\mathbf{r}) \simeq 0$. X-ray topographs of such defects have been recorded with the symmetrical 220, $2\bar{2}0$, 040 and $0\bar{4}0$ transmission reflections. Fig. 9 shows the two in-plane components $u_1(\mathbf{r})$ and $u_2(\mathbf{r})$ of the relative displacement field, reconstructed from such a series of topographs. This reconstruction corresponds well to a spherical defect with a deformation field of the form $u_i(x_1, x_2) = \varepsilon x_i/(x_1^2 + x_2^2)^n$, where the 'strength' of the defect ε and the exponent n can in principle be determined from the reconstructed relative displacement field.

6. Discussion

6.1. *SIMOX*

For standard SIMOX wafers, typically values of $\langle \varepsilon_{ii}(\mathbf{r}) \rangle = 5 \times 10^{-8}$ $(i = 1, 2)$ are found for the dilational distortion between the layer and the substrate, and values about ten times less for the rotation and shear components. This means that the difference between the two crystal lattices is mainly related to a tetragonal distortion in the range of several 10^{-8}. Moreover, to produce an in-plane lattice-parameter difference of, for example, 5×10^{-8} on a SIMOX wafer of 10 cm in diameter, one border of the layer must be moved by $5 \times 10^{-8} \times 10$ cm $= 50$ Å relative to the substrate, while the other border is fixed. Thus, during the annealing processes, the SiO_x layer of the SIMOX structure must allow a plastic flow of the layer over such distances. 'Pinholes' (remaining Si channels through the SiO_x layer) would inhibit, at least locally, such a flow and thus disturb the high symmetry of the relative displacement field $\mathbf{u}(\mathbf{r})$. One can conclude that no pinholes are present in the studied samples.

6.2. *Moiré topography*

The possibilities of the moiré topography can also be discussed in comparison with the 'usual' diffraction topography. For both methods, the same experimental set-up can be used, the first with single crystals, the second with bicrystals and both provide information

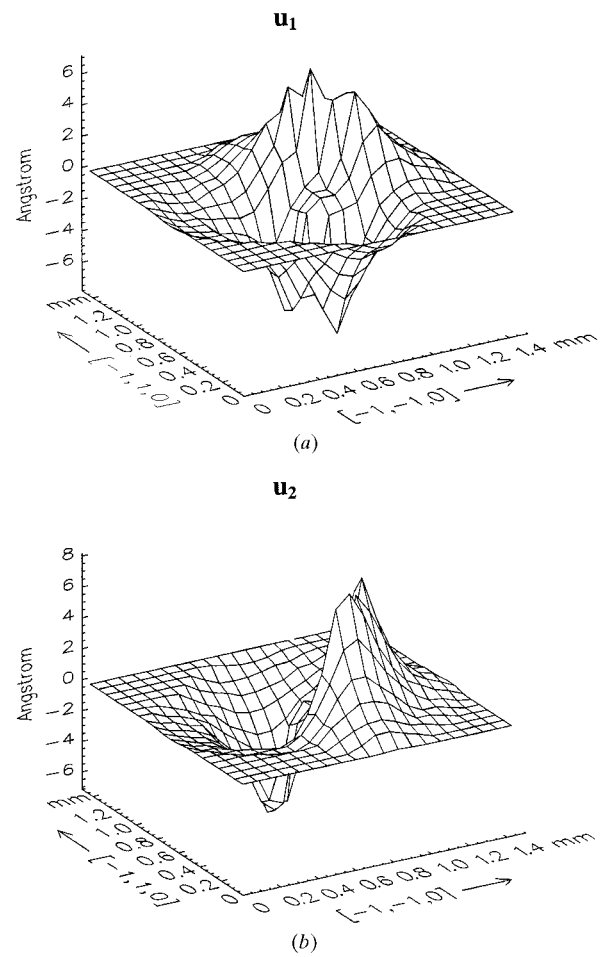

Fig. 9. The components $u_1(\mathbf{r})$ and $u_2(\mathbf{r})$ reconstructed from a 040 transmission topograph like that presented in Fig. 5 and of 220, $2\bar{2}0$, $0\bar{4}0$ topographs also recorded from this defect.

about the deformation tensor $\varepsilon_{ij}(\mathbf{r})$ and the atomic displacement field $\mathbf{u}(\mathbf{r})$. The 'usual' X-ray topography is sensitive to deformations $\varepsilon_{ij}(\mathbf{r})$ down to about 10^{-6}–10^{-7} and only for special cases can a higher sensitivity be achieved. An analysis of moiré fringes on topographs of bicrystals can cover the range from about 10^{-5} to 10^{-9} depending on the field of view and on the reflection used.

The spatial resolution of $\varepsilon_{ij}(\mathbf{r}_{||})$ and $\mathbf{u}(\mathbf{r}_{||})$ obtained from 'usual' topographs is limited by the diffraction process and cannot be better than about 1 μm. However, the high sensitivity achieved with moiré topography is paid for with a reduced spatial resolution as the information is averaged over an area that is half a moiré fringe distance for the method proposed in this article. Typical moiré-fringe distances are in the range between about 100 μm and several millimetres. This resolution can be increased when the profile of the moiré fringes is also used for the analysis but it is questionable whether the limit of 1 μm can be reached.

In some cases, both the 'usual' and the moiré topographies allow a direct reconstruction of the deformation or displacement fields from the contrast on sets of topographs (inverse problem, direct back-calculation). To also compare the two techniques in this respect, we assume, firstly, an experimental method employing monochromatic and highly collimated radiation, secondly, locally perfect crystals and bicrystals with a negligible depth dependency of the deformation field and, thirdly, plane-parallel surfaces and interfaces. Then, 'usual' and moiré topographs provide information about the crystal properties along $\mathbf{r}_{||}$ parallel to the surface.

On 'usual' topographs of locally perfect single crystals, the diffracted intensity $I(\mathbf{r}_{||})$ is then given by the local shift of the Bragg angle, the effective misorientation $\delta\Theta(\mathbf{r}_{||})$ (Authier, 1967). For a given reflection, up to six of the nine components of the deformation tensor may contribute to this quantity. As $\delta\Theta(\mathbf{r}_{||})$ is measured with respect to the lattice planes of a perfect reference part of the crystal, by changing the reflecting lattice planes, in principle all nine components of the deformation tensor $\varepsilon_{ij}(\mathbf{r}_{||})$ could be determined. The displacement field $\mathbf{u}(\mathbf{r}_{||})$ of the deformed crystal can then be calculated by an integration over the components of the deformation tensor.

On moiré topographs of locally perfect bicrystals, $I(\mathbf{r}_{||})$ is given by the moiré phase $\Phi_M(\mathbf{r}_{||})$. The moiré phases on at least three topographs directly provide the $u_i(\mathbf{r}_{||})$ but are given with reference to the interface plane between the two crystals. Therefore, even by changing the reflections, only six of the nine $\varepsilon_{ij}(\mathbf{r}_{||})$ can be determined from the experiment.

7. Summary and conclusions

A method has been developed for the quantitative analysis of moiré fringes on X-ray diffraction topographs. With this method, an analysis of moiré fringes allows one to reconstruct the relative displacement field between the two parts of a bicrystal with a high sensitivity on the basis of the contrast distribution in a set of topographs. It has been found that, for the studied SIMOX samples, the fringes were mainly due to a tetragonal deformation between the unit cells of layer and substrate and to a cylindrically symmetric relative displacement, perpendicular to the sample surface, between layer and substrate. A reconstruction of the relative displacement field between two parts of a bicrystal is of more than just academic interest: for example, in the present article it could be concluded that no pinholes are present in the studied SIMOX samples and that the SiO_x layer must allow plastic flow during the annealing process. Finally, the relative displacement fields around crystal defects can also be reconstructed from the moiré fringes and thus the proposed method is a powerful tool in the characterization of bicrystals and their defect structure.

The SOITEC company (Grenoble) is gratefully acknowledged for providing the SIMOX wafers. We also acknowledge Rolf Köhler and Jane Richter from the Humboldt Universität in Berlin for discussions and for recording some of the presented topographs.

References

Authier, A. (1967). *Adv. X-ray Anal.* **10**, 9–31.
Badaw, M. H. & Anand, K. V. (1977). *J. Phys. D.* **10**, 1931–1942.
Bonse, U. & Hart, M. (1965). *Appl. Phys. Lett.* **6**, 155–156.
Bowen, D. K. & Tanner, B. K. (1998). *High Resolution X-ray Diffraction and Topography.* New York: Taylor and Francis.
Chikawa, J. (1965). *Appl. Phys. Lett.* **7**, 193–195.
Haroutyunyan, V. S. (1996). *Crystallogr. Rep.* **41**, 915–920.
Haroutyunyan, V. S. & Sedrakyan, A. G. (1997). *Acta Cryst.* A**53**, 410–414.
Hart, M. (1972). *Philos. Mag.* **26**, 821–831.
Hart, M. (1975). *Proc. R. Soc. London Ser. A*, **346**, 1–22.
Jenichen, B., Köhler, R. & Möhling, W. (1985). *Phys. Status Solidi A*, **89**, 79–87.
Jenichen, B., Köhler, R. & Möhling, W. (1988). *J. Phys. E*, **21**, 1062–1066.
Jiang, B. L., Shimura, F. & Rozgonyi, G. A. (1990). *Appl. Phys. Lett.* **56**, 352–354.
Lang, A. R. (1968). *Nature (London)*, **220**, 652–657.
Ohler, M. & Härtwig, J. (1999). *Acta Cryst.* A**55**, 413–422.
Ohler, M., Prieur, E. & Härtwig, J. (1996). *J. Appl. Cryst.* **29**, 568–573.
Prieur, E. & Cloetens, P. (1996). Unpublished results.
Prieur, E., Guilhalmenc, C., Härtwig, J., Ohler, M., Garcia, A. & Aspar, B. (1996). *J. Appl. Phys.* **80**, 2113–2120.
Prieur, E., Ohler, M. & Härtwig, J. (1996). *Phys. Status Solidi A*, **158**, 19–34.
Veneables, D., Jones, K. S. & Namavar, F. (1992). *Appl. Phys. Lett.* **60**, 3147–3149.
Yoshimura, J. (1991). *Phys. Status Solidi A*, **125**, 429–440.
Yoshimura, J. (1996*a*). *Acta Cryst.* A**52**, 312–325.
Yoshimura, J. (1996*b*). *J. Appl. Phys.* **80**, 2138–2141.